Surfaces and Interfaces 98 (2026) 110279

Contents lists available at ScienceDirect

Surfaces and Interfaces

journal homepage: www.sciencedirect.com/journal/surfaces-and-interfaces

Real-time probing of adsorption dynamics on Pt nanoparticles: Competitive interactions and site blocking in electrocatalysis

Bruna Ferreira Gomes [a,*,1], Rameshwori Loukrakpam [a,*,1], Carlos M.S. Lobo [a], Tomas Bystron [b], Martin Prokop [b], Rodrigo Q. Albuquerque [c,d], Lu Xia [e], Wulyu Jiang [e], F. Pelayo García de Arquer [e], Karel Bouzek [b], Christina Roth [a]

[a] Electrochemical Process Engineering, University of Bayreuth, Universitätsstraße 30, 95447, Bayreuth, Bayern, Germany
[b] Department of Inorganic Technology, University of Chemistry and Technology Prague, Technicka 5, 16628, Prague 6, Czech Republic
[c] Department of Polymer Engineering, University of Bayreuth, Universitätsstraße 30, 95447, Bayreuth, Bayern, Germany
[d] Neue Materialien Bayreuth GmbH, Gottlieb-Keim-Straße 60, 95448, Bayreuth, Bayern, Germany
[e] ICFO-Institut de Ciències Fotòniques, The Barcelona Institute of Science and Technology, Castelldefels (Barcelona), 08860, Spain

ARTICLE INFO

Keywords:
Surface dynamics
Fixed Energy X-ray Absorption Voltammetry
$\Delta\mu$XANES
Machine Learning
Operando X-ray Absorption Spectroscopy
Competitive Adsorption
Site Blocking
Electrocatalyst Poisoning

ABSTRACT

Electrochemical energy conversion involves both steady-state and transient phenomena, with the latter being difficult to probe under realistic conditions. Conventional in-situ/operando X-ray absorption spectroscopy often lacks time resolution and provides mainly qualitative insights. In this study, we show that the $\Delta\mu$ XANES method, applied on the Pt/H_3PO_3 system, enables potential-dependent tracking of surface speciation and relative changes in adsorbate populations. It distinguishes H_3PO_3 concentrations and reveals competition for Pt sites among O-, H-, CO-, H_3PO_3- and H_3PO_4-derived species. Despite XAS being bulk-sensitive, $\Delta\mu$ yields indirect yet reliable surface information. Coupled with time-resolved fixed-energy X-ray absorption voltammetry (FEXRAV), the transient evolution of the Pt electronic structure is monitored during CO stripping, revealing dynamic electronic changes that precede the maximum electrochemical oxidation current. The complementary use of FEXRAV and $\Delta\mu$ XANES correlates these transient electronic responses with the underlying surface speciation, providing mechanistic insight into competitive adsorption on Pt. Machine learning validation confirms predictive power despite low signal-to-noise ratio. This establishes the combination of $\Delta\mu$ XANES and FEXRAV as a versatile tool for probing interfacial dynamics in fuel cells, electrolyzers, and CO_2 reduction technologies that can be readily implemented at conventional XAS beamlines.

1. Introduction

The global transition to renewable energy relies heavily on electrochemical processes for large-scale applications, including fuel cells, electrolyzers, direct N_2 and CO_2 reduction, and photoelectrochemistry. Achieving this goal requires a detailed atomic-level understanding of electrocatalytic processes at the catalyst interface [1–3]. Significant progress has been made in real-time visualization of electrochemical interfaces, supported by advanced methods with improved temporal and lateral resolution, often coupled with artificial intelligence to deepen mechanistic insights into efficient electrocatalysis [4–12]. Among the wide range of analytical techniques, X-ray absorption spectroscopy (XAS) has emerged as a powerful tool to probe electrocatalysts under relevant conditions.

Numerous ex-situ studies using X-ray absorption near edge structure (XANES) and extended X-ray absorption fine structure (EXAFS) on electrocatalysts are reported in the literature [8,13,14]. However, these focus on quasi-steady-state systems that do not reflect the dynamic rearrangements, multiple active sites, and complex adsorption patterns present under operating conditions, where the key reaction intermediates are formed and consumed on very short timescales and which traditional XAS cannot resolve. For this reason, in-situ and operando approaches have gained significant attention for detecting these short-lived reaction intermediates thereby revealing reaction mechanisms [9, 15–29]. Time-resolved methods such as QEXAFS and energy-dispersive XAS (EDXAS) have provided insights into electrochemical reaction kinetics (such as oxygen reduction or hydrogen evolution reactions), achieving sub-second resolution [30–37]. Despite their value, these

* Corresponding authors.
E-mail addresses: bruna.lobo@uni-bayreuth.de (B. Ferreira Gomes), rameshwori.jalan@uni-bayreuth.de (R. Loukrakpam).
[1] These authors contributed equally.

https://doi.org/10.1016/j.surfin.2026.110279
Received 22 April 2026; Received in revised form 29 July 2026; Accepted 1 August 2026
Available online 24 August 2026
2468-0230/© 2026 The Authors. Published by Elsevier B.V. This is an open access article under the CC BY license (http://creativecommons.org/licenses/by/4.0/).

techniques remain limited by data volume, narrow energy ranges, operando constraints, and the requirement for dedicated instrumentation available at only a limited number of synchrotron beamlines. Consequently, there remains a need for practical and broadly accessible time-resolved approaches that can be readily implemented at conventional XAS beamlines while providing simultaneous information on catalyst states and adsorbates under dynamic electrochemical conditions. More recently, attention has therefore turned to two complementary approaches: fixed energy X-ray absorption voltammetry (FEXRAV), [38–57] and the $\Delta\mu$ XANES method [4,58–61] which, when used together, enable tracking a catalyst's transient electronic responses and identification of surface adsorbates under realistic conditions. Originally developed by Ramaker and co-workers, the $\Delta\mu$ XANES methodology uses a reference spectrum acquired in the electrochemical double-layer region, where the Pt surface exhibits a relatively stable composition and no significant faradaic processes occur. Difference spectra generated relative to this reference are then interpreted through comparison with FEFF-calculated fingerprints, enabling the identification of surface adsorbates and their adsorption geometries [4].

While these methodological developments have significantly expanded the scope of operando XAS, their application to technologically relevant systems such as high-temperature proton exchange membrane fuel cells (HT-PEMFCs) remains limited, particularly in resolving competitive adsorption processes under dynamic electrochemical conditions. In particular, there is a need to correlate the dynamic evolution of adsorbates and time-resolved electronic responses in systems where multiple species simultaneously interact with the catalyst surface and transient effects play a decisive role. HT-PEMFCs use polybenzimidazole (PBI) membranes imbibed with H_3PO_4 for proton conduction at temperatures above 120 °C. Under realistic operating conditions, H_3PO_4 can leach out and either adsorb strongly on Pt catalytic sites, thereby slowing down electrode kinetics, or be reduced to H_3PO_3 at the anode in the presence of H_2 at lower electrode potentials [62–64]. Both H_3PO_3 and CO — another well-known poisoning species in PEMFCs — compete for Pt active sites and get oxidized in similar potential ranges [5,65]. Despite its recognized formation in HT-PEMFCs, the competitive adsorption behavior of H_3PO_3 and its influence on hydrogen adsorption remain insufficiently understood. Establishing these fundamental adsorption mechanisms in a controlled half-cell configuration at 25 °C is a necessary step toward future operando investigations under realistic HT-PEMFC conditions. In our previous work, we identified these adsorbed species on Pt/C using $\Delta\mu$ XANES, establishing their spectroscopic fingerprints under steady-state conditions but without addressing the relation between $\Delta\mu$ signal intensity, surface coverage, and competitive site occupation. In the present study, we extend our previous qualitative identification approach [5] by systematically correlating changes in $\Delta\mu$ XANES intensity with electrochemical observables, allowing relative changes in surface speciation and competitive adsorption to be tracked. By integrating steady-state $\Delta\mu$ XANES for surface speciation with FEXRAV for tracking transient Pt-specific electronic responses during potential cycling, we investigate the dynamic evolution of competitive adsorption under controlled electrochemical conditions. This combined approach enables direct insight into adsorption, site blocking, and removal processes involving H, CO, O-, and H_3PO_3-derived species under controlled electrochemical conditions.

Importantly, although XAS is typically regarded as a bulk-sensitive technique, we show that $\Delta\mu$ XANES enables the extraction of indirect yet reliable information on surface composition under conditions where soft-XAS or X-ray photoelectron spectroscopy (XPS) would be restricted due to vacuum requirements and limited catalyst loading. Finally, we evaluate the consistency of the observed relationships between experimental conditions and spectroscopic responses using machine learning procedures capable of predicting $\Delta\mu$ XANES features under specific conditions. The model was trained not only on the Pt/C data presented here but also on Pt alloys, confirming the systematic nature of the observed trends and highlighting the potential for extension to non-noble metal catalysts. This establishes a powerful and versatile framework for probing adsorption dynamics under realistic electrochemical conditions, broadly applicable to key electrochemical energy conversion reactions.

2. Results and discussion

Dynamic changes on Pt catalyst surface revealed by Fixed Energy X-ray Absorption Voltammetry (FEXRAV)

Fixed-Energy X-ray Absorption Voltammetry (FEXRAV) was employed to follow transient Pt-specific electronic responses during the electrochemical measurements. As summarized in Fig. 1, the fluorescence intensity at a selected energy within the Pt L_3-edge white-line region (11,568 eV) was recorded continuously during cyclic voltammetry and correlated with the applied electrode potential. The time derivative of the fluorescence signal, $\left(\frac{dFluo}{dt}\right)$, highlights potential regions in which the Pt X-ray absorption changes most rapidly, providing an element-specific voltammetry-like profile that can be directly compared with features observed in the electrochemical response [66]. Unless otherwise explicitly stated, the term "FEXRAV analysis" refers throughout this work to the analysis based on $\left(\frac{dFluo}{dt}\right)$. A detailed description of the energy selection, signal synchronization, alignment, interpolation, and data treatment is provided in the Experimental Section.

First CV cycle: CO stripping

Fig. 2 compares the cyclic voltammograms and the corresponding FEXRAV responses recorded during the first anodic cycle, in which the Pt surface is initially saturated with adsorbed CO. In the absence of H_3PO_3, the anodic scan exhibits the characteristic CO stripping peak in the CV (Fig. 2A), while the corresponding FEXRAV response (Fig. 2B) displays a pronounced negative feature in the same potential region. The FEXRAV profile reproduces not only the position of the CO oxidation process but also the two shoulders observed in the electrochemical response, demonstrating that the derivative treatment provides an element-specific voltammetric-like signal closely following the Pt-related electrochemical transformation while suppressing contributions from parallel processes that do not significantly modify the Pt electronic structure.

The negative-going FEXRAV feature should not be interpreted simply as a reduction of Pt. Instead, it represents the rapid electronic reorganization of the Pt surface accompanying CO removal. During this process, several phenomena occur simultaneously, including the disappearance of Pt–CO bonds, changes in the occupation of Pt 5d states, adsorption of oxygenated species (OH), the onset of Pt oxide formation, and the associated modification of the Pt L_3-edge spectral shape. Together, these changes produce a substantial decrease in the fluorescence intensity at the selected fixed energy, resulting in the intense negative derivative observed during CO stripping. This interpretation is consistent with the $\Delta\mu$ XANES measurements, discussed in detail in Section "Steady state adsorbed species on Pt catalyst surface", which showed that CO adsorption produces a significantly larger spectral modification than H_3PO_3 adsorption under equivalent conditions.

Beyond the CO stripping region, a small positive feature appears at approximately 0.95–1.0 V (Fig. 2B). Since this signal occurs within the potential range where Pt oxide formation is expected, and oxide formation is known to increase the Pt L_3-edge white-line intensity, this feature is assigned to the initial formation of Pt–O species.

During the cathodic scan, the positive FEXRAV response observed in the H_{upd} region coincides with hydrogen adsorption on Pt. This result indicates that hydrogen adsorption also modifies the Pt electronic structure sufficiently to produce a measurable change in the fluorescence intensity, although substantially smaller than that associated with CO removal.

When 200 μmol L^{-1} H_3PO_3 is added (Fig. 2C and D), the negative FEXRAV feature becomes less intense and loses one of its shoulders,

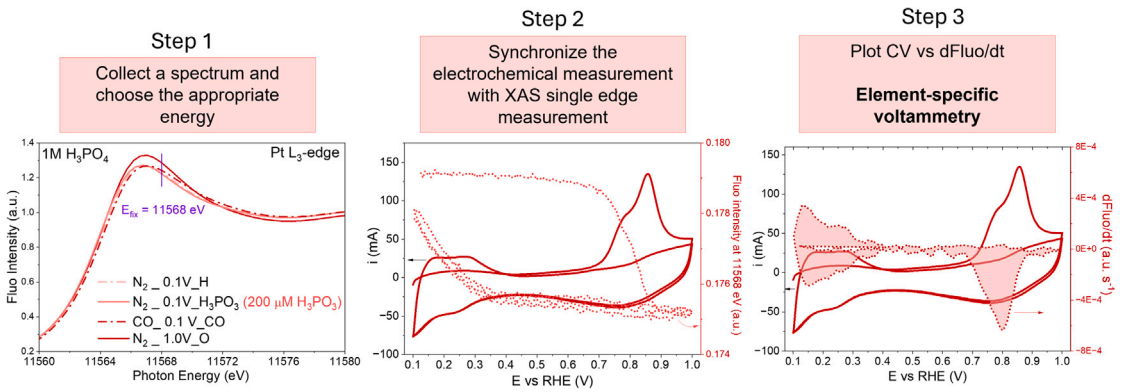


Fig. 1. Diagram illustrating the FEXRAV method from fixed-energy selection to the generation of the element-specific voltammetric-like signal ($dFluo/dt$ vs. potential). The fixed energy point to follow (E_{fix}) was chosen to be 11,568 eV.

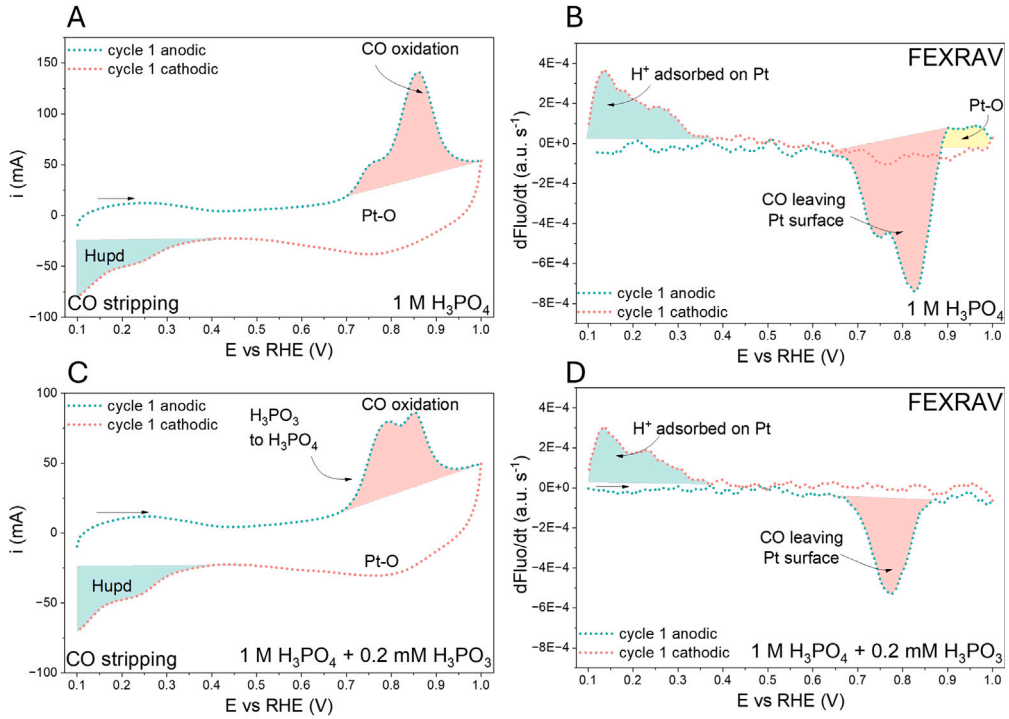


Fig. 2. Comparison between cyclic voltammetry and FEXRAV during the first CO stripping cycle. (A) Cyclic voltammogram recorded in 1 mol L^{-1} H_3PO_4 after CO adsorption. (B) Corresponding FEXRAV response obtained from the time derivative of the fluorescence intensity measured at the Pt L_3-edge. (C) Cyclic voltammogram recorded in 1 mol L^{-1} H_3PO_4 containing 200 μmol L^{-1} H_3PO_3 after CO adsorption. (D) Corresponding FEXRAV response. Shaded regions highlight the Pt-related electrochemical processes identified by both techniques.

closely following the modification observed in the CO stripping voltammogram. Simultaneously, the positive feature associated with Pt oxide formation is no longer detected, while the hydrogen adsorption response also decreases in intensity. These observations indicate that H_3PO_3 modifies the adsorption of CO and alters the distribution of available Pt surface sites, while simultaneously suppressing Pt oxide formation within the detection limits of the FEXRAV measurement.

Second CV cycle: CO-free surface

The second voltammetric cycle (Fig. 3) was recorded after complete removal of the adsorbed CO layer and therefore reflects only the intrinsic surface processes occurring on Pt.

In the absence of H_3PO_3 (Fig. 3A and B), the anodic scan begins with hydrogen desorption, which appears as a negative FEXRAV feature due to the decrease in fluorescence intensity accompanying the removal of adsorbed hydrogen. At higher potentials, the fluorescence derivative becomes positive, consistent with the formation of Pt oxide. During the subsequent cathodic scan, the FEXRAV signal becomes negative in the potential region corresponding to Pt oxide reduction and subsequently increases again within the H_{upd} region, where hydrogen is readsorbed onto the Pt surface. The close correspondence between the electrochemical and spectroscopic responses confirms that FEXRAV selectively follows the electronic changes occurring on the Pt surface throughout the complete voltammetric cycle.

In the presence of 200 μmol L^{-1} H_3PO_3 (Fig. 3C and D), the FEXRAV features associated with Pt oxide formation and reduction are no longer observed, indicating that H_3PO_3 strongly suppresses oxide formation under the investigated conditions. In contrast, the hydrogen adsorption and desorption features remain detectable, although both exhibit reduced intensity and modified shape. In particular, the hydrogen desorption region changes from two well-defined shoulders in the absence of H_3PO_3 to a single broader feature when H_3PO_3 is present. This behavior indicates that H_3PO_3 alters the distribution of Pt surface

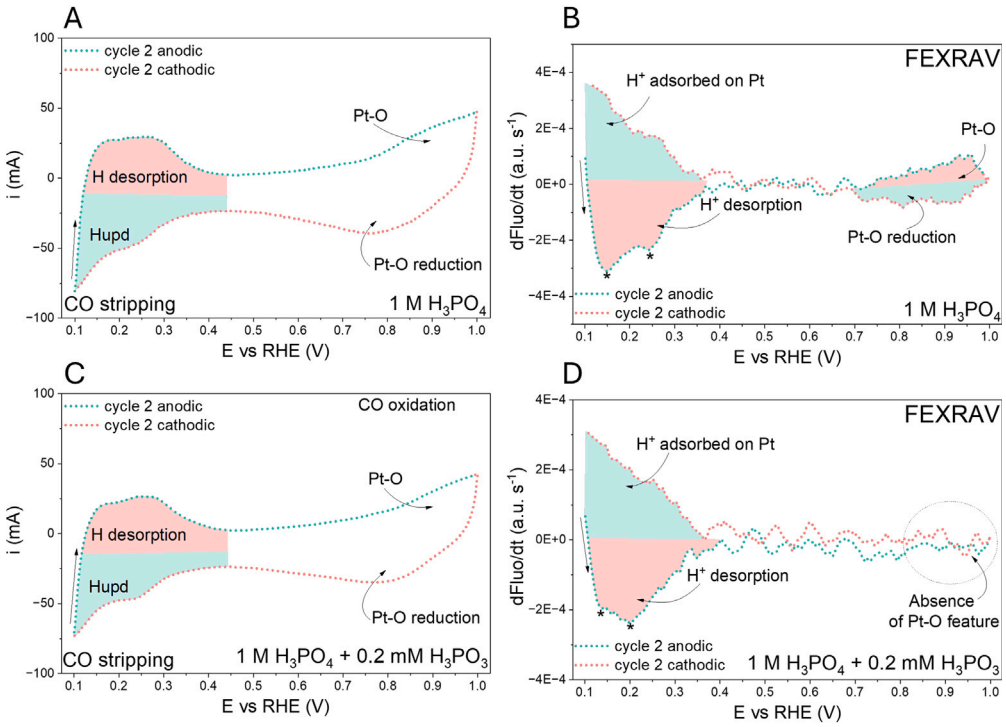


Fig. 3. Comparison between cyclic voltammetry and FEXRAV during the second voltammetric cycle after complete removal of adsorbed CO. (A) Cyclic voltammogram recorded in 1 mol L^{-1} H_3PO_4. (B) Corresponding FEXRAV response obtained from the time derivative of the fluorescence intensity measured at the Pt L_3-edge. (C) Cyclic voltammogram recorded in 1 mol L^{-1} H_3PO_4 containing 200 μmol L^{-1} H_3PO_3. (D) Corresponding FEXRAV response. The disappearance of the Pt oxide-related FEXRAV features in the presence of H_3PO_3 indicates suppression of Pt oxide formation, while the modified H_{upd} adsorption/desorption features reveal changes in the distribution of active Pt surface sites.

sites participating in hydrogen adsorption, consistent with competitive adsorption between hydrogen and phosphorous-containing species.

***FEXRAV analysis of competitive adsorption and Pt surface poisoning by* H_3PO_3**

One of the initial motivations of this work was to evaluate whether FEXRAV could track the evolution of Pt surface poisoning by H_3PO_3 through changes in the integrated signal and to compare these changes with those obtained from the corresponding integrated electrochemical response. Since adsorption of H_3PO_3 also modifies the CO stripping response, both the H_{upd} and CO stripping regions were investigated by comparing the integrated cyclic voltammetry signals with the corresponding integrated FEXRAV responses (Figure S1).

Although both techniques clearly respond to the presence of H_3PO_3, the evolution of the integrated signals differs substantially. In the cyclic voltammograms, the CO stripping charge initially increases after the first addition of H_3PO_3, followed by a progressive decrease with increasing concentration. The H_{upd} charge shows a non-monotonic response to increasing H_3PO_3 concentration, with slight variations at low H_3PO_3 concentrations followed by a stark decrease at higher concentrations. In contrast, the integrated FEXRAV signals do not follow the same trend. The H_{upd}-related contribution exhibits only a slight increase at low concentrations before decreasing sharply at the highest concentrations, whereas the CO stripping contribution decreases rapidly during the first additions of H_3PO_3, remains nearly constant over the intermediate concentrations, and decreases again at the highest concentration.

These observations demonstrate that, despite the close qualitative correspondence between cyclic voltammetry and FEXRAV, the two techniques probe different physical quantities. Cyclic voltammetry measures the overall faradaic response, whereas the $\frac{dFluo}{dt}$ signal reflects the magnitude and rate of the electronic changes occurring at the Pt atoms monitored at the selected X-ray energy. Consequently, identical changes in electrochemical charge do not necessarily produce proportional changes in the FEXRAV response.

To better understand these differences, the individual cyclic voltammograms and FEXRAV profiles obtained at each H_3PO_3 concentration are presented separately in Figure S2. Both techniques show progressive modifications of the two characteristic CO stripping contributions. In the cyclic voltammograms, the relative intensity of the two peaks changes with increasing H_3PO_3 concentration, accompanied by small positive shifts in their peak potentials. In contrast, the corresponding FEXRAV features appear systematically at potentials approximately 10–30 mV lower than the respective electrochemical peaks and exhibit considerably larger shifts with increasing H_3PO_3 concentration. Considering the estimated synchronization uncertainty of approximately ±3.3 mV (or ±6.7 mV under the conservative assumption of a full acquisition interval), these offsets cannot be explained solely by uncertainty in the temporal alignment procedure.

The lower potential of the FEXRAV response suggests that modifications of the Pt electronic structure begin before the maximum faradaic oxidation current is reached. This behavior is consistent with the fact that, during CO stripping, adsorption of oxygenated species, particularly OH, precedes complete CO oxidation to CO_2. Since these oxygenated intermediates modify the electronic structure of Pt before the electrochemical oxidation reaches its maximum rate, FEXRAV detects the onset of these electronic changes earlier than the current maximum observed in cyclic voltammetry.

To further investigate the origin of these two contributions, both the electrochemical and FEXRAV peaks were deconvoluted into two individual components (Figures S3 and S4), and the corresponding peak positions and integrated areas are summarized in Figure S5. According to previous studies on polycrystalline Pt, the lower-potential contribution, centered near 0.75 V vs RHE, is predominantly associated with CO oxidation on low-coordinated Pt sites, such as (100)- and (110)-like domains, whereas the higher-potential contribution near 0.85 V is mainly attributed to Pt(111) terrace sites, where CO is more strongly stabilized [67,68].

The electrochemical peak areas show that the low-potential contribution increases with H_3PO_3 concentration, whereas the high-potential contribution initially increases after the first addition and then decreases markedly at higher concentrations. This behavior suggests that competition with H_3PO_3 preferentially displaces CO from low-coordinated Pt sites, leading to the redistribution of the remaining adsorbed CO toward Pt(111)-like terraces. The FEXRAV-derived peak areas reveal a preferential suppression of the low-potential contribution but with a markedly different evolution. The low-potential FEXRAV feature progressively disappears as the concentration of H_3PO_3 increases, indicating that removal of CO from these sites no longer produces a significant electronic perturbation because they become preferentially occupied by H_3PO_3. Since $\Delta\mu$ XANES measurements (discussed in Section "Steady state adsorbed species on Pt catalyst surface") demonstrated that CO adsorption produces a substantially larger modification of the Pt L_3-edge than H_3PO_3, replacement of CO by H_3PO_3 naturally results in a much weaker FEXRAV response.

In contrast, the higher-potential FEXRAV feature initially persists and reaches a maximum near 1×10^{-4} mol L^{-1} before decreasing at 2×10^{-4} mol L^{-1}. This behavior is consistent with an initial redistribution of CO toward Pt(111)-like terrace sites after preferential occupation of the low-coordination sites by H_3PO_3. Once these preferential sites become saturated, H_3PO_3 begins to compete with CO for adsorption on the terrace sites as well, leading to the subsequent decrease of the higher-potential contribution. Together, these results demonstrate that FEXRAV provides complementary information to conventional electrochemistry by directly revealing how adsorption-induced modifications of the Pt electronic structure evolve during competitive adsorption, rather than simply following the overall electrochemical charge.

Although competitive adsorption provides a consistent explanation for the experimental observations, additional processes may also contribute to the Pt surface changes observed during CO stripping. In particular, one such process is the direct chemical interaction between H_3PO_3 and oxygenated Pt surface species. Previous electrochemical studies have shown that H_3PO_3 can react with PtO_x surface species, consuming surface oxides while being oxidized to H_3PO_4, thereby shifting the equilibrium toward reduced Pt [63]. Although the present experiments do not allow the contribution of this process to be quantified, it may partially reinforce the suppression of oxygenated Pt species observed throughout this work. Taken together, the experimental observations are most consistently explained by competitive adsorption. Adsorbed H_3PO_3 may reduce the availability of Pt sites involved in Pt-OH formation, thereby decreasing the population of reactive Pt–CO/Pt–OH ensembles required for CO oxidation through the Langmuir–Hinshelwood mechanism [68]. At the same time, H_3PO_3 competes directly with CO for adsorption sites, redistributing the remaining CO over the Pt surface.

In the present data, these effects are primarily reflected by changes in the relative peak areas and by an increasing separation between the FEXRAV and electrochemical peak potentials, rather than by a pronounced positive shift of the high-potential CO stripping peak. In particular, the progressive shift of the high-potential FEXRAV contribution toward lower potentials indicates that the electronic reorganization of the remaining CO-covered Pt sites begins earlier as the concentration of H_3PO_3 increases. Since the corresponding CV peak remains nearly unchanged at approximately 0.85–0.86 V vs. RHE, these electronic changes precede the maximum faradaic rate of CO oxidation and should not be interpreted as an earlier conversion of CO to CO_2. Instead, the results suggest that FEXRAV detects the onset of Pt electronic structure modifications associated with competitive adsorption and the formation of oxygenated intermediates before the electrochemical oxidation current reaches its maximum. Together, these findings suggest that the poisoning effect of H_3PO_3 extends beyond simple site blocking. By influencing the formation of oxygenated Pt species, H_3PO_3 may also modify the surface reaction pathways responsible for catalyst activity.

While FEXRAV provides time-resolved, element-specific information on the evolution of the Pt electronic structure during potential cycling, the measured response reflects the combined effect of several concurrent processes, including CO removal, hydrogen adsorption, Pt oxidation, and adsorbate-induced modifications of the Pt electronic structure. Consequently, although FEXRAV reveals when these electronic changes occur and how their intensity evolves with H_3PO_3 concentration, it does not directly identify the surface species responsible for each contribution. To obtain this information, complementary $\Delta\mu$ XANES measurements were performed. Unlike FEXRAV, which follows the kinetics of the electronic response, $\Delta\mu$ XANES provides potential-dependent snapshots of the Pt surface under well-defined electrochemical conditions, allowing the contributions from adsorbed CO, hydrogen, oxygenated species, and H_3PO_3 to be distinguished. The combination of both techniques therefore enables correlation of the dynamic FEXRAV features with the underlying surface speciation, providing a comprehensive picture of the competitive adsorption processes occurring on the Pt surface.

Steady state adsorbed species on Pt catalyst surface ($\Delta\mu$ XANES)

In contrast to our earlier work [5], where $\Delta\mu$ XANES was employed primarily to assign spectroscopic fingerprints to individual adsorbates, the focus here shifts toward tracking relative changes in adsorbate populations through variations in $\Delta\mu$ signal intensity. By systematically varying the H_3PO_3 concentration and correlating the resulting $\Delta\mu$ XANES features with electrochemical observables and the transient electronic response obtained by FEXRAV, we demonstrate that relative changes in $\Delta\mu$ amplitude reflect changes in surface speciation and competitive site occupation. This approach enables discrimination not only between different adsorbed species, but also between their relative contributions under single-adsorbate and competitive adsorption conditions.

The results presented in Fig. 4 show the intensity of the $\Delta\mu$ XANES signal as a function of the concentration of H_3PO_3 in a 1 mol L^{-1} H_3PO_4 electrolyte, with a Pt/C catalyst, at three different potentials. The three potentials were selected because the following adsorbed species are predominantly present on the Pt surface at these potentials: H at 0.1 V, H_3PO_3 at 0.5 V, and O at 1 V. The $\Delta\mu$ XANES features were compared with $\Delta\mu$ spectra calculated using FEFF (dotted lines). To follow the changes in intensity with increasing concentrations of H_3PO_3, the simulated characteristic signatures of H, H_3PO_3, and O are added for comparison. The same experiment was conducted in the presence of CO to evaluate the competition for active sites between CO and H_3PO_3. Since the binding energies of CO are well-known, the comparison between single and competitive adsorption allowed for the elucidation of H_3PO_3 adsorption [69].

At more negative potentials within the range of the CV, the adsorption of H on the Pt surface is expected. According to Fig. 4A (see also Figure S8), the characteristic feature (which swings from negative to positive as the relative energy E increases) is anticipated for H adsorption, while the presence of H_3PO_3 (adsorbed in its tetrahedral form, see Figure S7) is observed with its own characteristic feature: a positive signal near 0 eV. It should be noted that accurately pinpointing the positions of $\Delta\mu$ features is quite challenging, and here we rely more on the relative positions of signals from different species. In this context, the presence of H_3PO_3 causes a reduction in the positive signal intensity (around the 10 eV region), while a new feature emerges around 0 eV, similar to the shape observed with the FEFF-simulated H spectrum.

At 0.5 V and therefore right within the double layer region (Fig. 4C and Figure S9), a minimal amount and constant coverage of adsorbed species is expected, as no faradaic processes are anticipated in this region. It is known that H_3PO_4 species or anion species from the electrolyte in general can be adsorbed in this potential range [5]. However, since the reference spectrum is obtained in 1 mol L^{-1} H_3PO_4

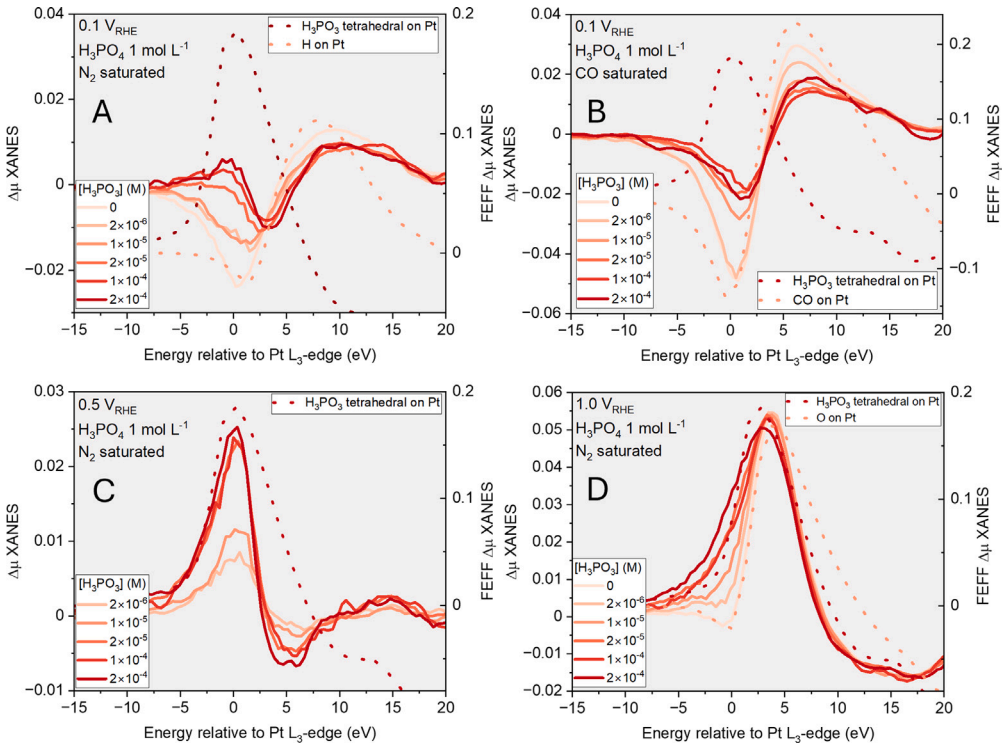


Fig. 4. $\Delta\mu$ XANES measurements were conducted at various potentials and different H_3PO_3 concentrations. The experiments were performed in electrolytes saturated with N_2 (A, C, and D) and CO (B). The measurements were performed at the following potentials: 0.1 V_{RHE} (A and B), 0.5 V_{RHE} (C), and 1.0 V_{RHE} (D). Dotted lines represent the FEFF-simulated characteristic signatures. The measurements were performed in 1 mol L^{-1} H_3PO_4 electrolyte with the addition of H_3PO_3. The corresponding $\Delta\mu$ XANES spectra for the datasets presented in Fig. 4 are shown in greater detail in the Supporting Information (Figures S8–S11), highlighting the evolution of the spectral features with increasing H_3PO_3 concentration. All measurements were performed in 1 mol L^{-1} H_3PO_4 electrolyte with the addition of H_3PO_3.

at 0.5 V, the features observed here are directly related to the adsorption of H_3PO_3 on Pt. Interestingly, the feature increases with rising H_3PO_3 concentration, reaching a maximum that likely corresponds to the formation of a stable multilayer on the Pt surface with a defined adsorption capacity, as previously reported for H_3PO_3 [63]. It is also important to note that at the highest studied concentration, 2×10^{-4} mol L^{-1}, the simulated $\Delta\mu$ feature indicates that H_3PO_3 adsorbs to Pt through P–O–Pt bonds, suggesting a tetrahedral structure motif. This is distinctly different from the adsorption of this species at relatively high concentrations (10^{-2} mol L^{-1}), [5] which predominantly adopts a pyramidal configuration (P–Pt). FEFF calculations for the two main possible configurations are shown in Figure S7.

At more positive potentials (Fig. 4D and Figure S10), the formation of Pt oxides is expected, hence the predominant feature is the adsorption of oxygen. According to FEFF simulations, this is characterized by a negative signal around 0 eV and a positive one around 5 eV. With the addition of H_3PO_3, a reduction in the intensity of the signal at 5 eV and a broadening in the region is observed, further indicating that H_3PO_3 is (co-)adsorbing and occupying active sites on Pt. This could explain the decrease in catalytic activity when the concentration of H_3PO_3 increases. Recently, it was shown that at this potential H_3PO_3 is oxidized to H_3PO_4 by water, while producing H_2 [63,70]. The progressive suppression of the oxygen-related $\Delta\mu$ feature with increasing H_3PO_3 concentration is consistent with the disappearance of the Pt oxide-related FEXRAV signal observed during the second voltammetric cycle, further supporting that H_3PO_3 inhibits Pt oxide formation under the investigated conditions.

In the presence of CO (Fig. 4B and Figure S11), a similar effect to that observed for H species is noted: the higher the concentration of H_3PO_3, the lower the intensity of the feature associated with CO, and the increase in intensity around 0 eV is characteristic of the presence of H_3PO_3. Compared with Fig. 4A, the feature associated with the H_3PO_3 species is not as evident within the range of 0.1 to 0.4 V. Therefore, even though there is a clear competition between CO and H_3PO_3, the H_3PO_3 species in its tetrahedral configuration (observed at low concentrations) has a lower adsorption energy than CO species, but definitely adsorbs stronger than H species. This interpretation is fully consistent with the FEXRAV results, where CO removal dominates the transient spectroscopic response owing to its much larger perturbation of the Pt L_3-edge compared to H_3PO_3. Consequently, adsorption of H_3PO_3 primarily modifies the intensity, position and relative contribution of the CO-related FEXRAV features through competitive adsorption rather than generating an equally intense spectroscopic signature of its own.

Machine learning predictions of XANES spectra

Given that traditional first-principles methods, such as DFT, are computationally demanding, and experimental XANES measurements are both costly and time-consuming, the use of machine learning (ML) models to predict XANES was explored. By leveraging ML, we aimed to develop a faster, data-driven approach to predict spectra based on experimental conditions, reducing the need for extensive measurements. The experimental conditions associated with the previously discussed XANES spectra served as inputs to train a ML model designed to predict the $\Delta\mu$ XANES spectra in the vicinity of the Pt edge (refer to the Methodology section for comprehensive details). We employed the random forests algorithm, as developed by Breiman, [71] for this task. Although prior research demonstrates successful use of ML models, for example in performing inverse design using datasets comprising approximately 30 experiments, [72] we expanded our dataset to enhance model accuracy. This decision is further motivated by the need to predict not merely a single data point, but a complete XANES spectrum (consisting of at least 7 data points). We incorporated additional experimental conditions and corresponding spectra from similar materials to refine our ML model further.

The model's performance was evaluated on all 16 curves of the test set, from which four selected XANES spectra are illustrated in Fig. 5. Because the XANES curves are continuous with a number of points per curve much higher than the dataset size of only 76 experiments, only selected points of the curves were used as ML features (circles vs. squares in Fig. 5). Overall, the model achieved for the test set a Mean Absolute Error (*MAE*) of 0.0058 and $R^2 = 0.88$. Comparing the test error with the training error ($MAE = 0.0031$, $R^2 = 0.97$) shows that some overfitting is present in the ML model employed. Further reducing overfitting via hyperparameter optimization is difficult due to the relatively small number of experiments in the current dataset. A detailed description of the predictions, training errors and variance analysis of the model is available in the Supporting Information. The available dataset comprises only 76 experiments, which inevitably limits the complexity of the ML model that can be trained without overfitting. Consequently, the present model should be regarded as a proof of concept demonstrating that meaningful relationships between experimental conditions and $\Delta\mu$ XANES spectra can already be learned from relatively limited experimental data. Within the experimental domain represented by the available data, the trained model generalizes to previously unseen combinations of experimental conditions. Expanding the dataset with additional catalyst compositions and operating conditions will be necessary to improve the model robustness and extend its applicability to chemically distinct catalyst systems.

Beyond the limitations imposed by the dataset size, it should be noted that the Random Forest model was trained exclusively on Pt-based catalyst systems, and the inclusion of Pt alloys was intended to improve predictive accuracy within this chemical space rather than to generalize across metal families. Consequently, the model's ability to predict $\Delta\mu$ XANES spectra for non-noble metal catalyst systems remains untested, and its current performance metrics (test MAE = 0.0058, R^2 = 0.88) should be interpreted as reflecting interpolation within Pt-based chemistry rather than extrapolation to fundamentally different electronic structures and adsorption mechanisms. The moderate gap between training and test error is consistent with the limited size of the dataset (76 experiments) rather than with memorization of specific spectral signatures, as the model retains substantial predictive power on held-out data. Nonetheless, extending this approach to non-noble metal systems would require dedicated experimental efforts to establish whether the learned relationships reflect transferable physical descriptors of the Pt L_3-edge response or are specific to Pt-based electronic structure.

Using ML for XANES prediction offers significant advantages, including faster and more efficient spectral predictions compared to computationally expensive first-principles methods and time-consuming experimental measurements. By reducing the need for extensive synchrotron beamtime, ML lowers costs while optimizing experimental conditions to achieve desired spectral features with minimal trial and error. Additionally, ML models extract valuable insights from the datasets, like feature importances, enhancing spectral interpretation and material characterization.

Beyond serving as a proof of concept, the machine-learning analysis presented here provides an independent validation of the adsorption trends extracted from $\Delta\mu$ XANES. By learning the relationship between experimental conditions and spectral response, the model confirms that the observed spectroscopic trends are systematic rather than anecdotal, despite the inherently low signal-to-noise ratio of operando $\Delta\mu$ XANES. The ML results further support the interpretation of the combined $\Delta\mu$ XANES and FEXRAV measurements by demonstrating that the spectroscopic response evolves consistently with the experimentally observed changes in surface speciation and Pt electronic structure. Importantly, this approach demonstrates the potential to predict spectroscopic responses prior to beamtime allocation, thereby extending the practical impact of the combined $\Delta\mu$ XANES–FEXRAV methodology.

3. Conclusion

Our results show that H_3PO_3 strongly blocks Pt active sites, competing with H and CO and suppressing oxygen adsorption, even at low concentrations. Beyond reducing the number of available active sites, H_3PO_3 also modifies their distribution, altering both the electrochemical response and the evolution of the Pt electronic structure. These findings highlight the critical role of phosphorus-derived contaminants in limiting HT-PEMFC performance and demonstrate the necessity of designing catalyst surfaces with enhanced resistance to such poisoning effects. The combined use of FEXRAV and $\Delta\mu$ XANES provides a comprehensive view of these competitive adsorption processes, by coupling transient electronic structure dynamics with direct information on surface speciation.

The unique capability of FEXRAV to follow transient changes in the Pt electronic structure in real time enabled the dynamic tracking of CO removal and its competition with H_3PO_3. Rather than reproducing the electrochemical current, FEXRAV selectively probes the magnitude and kinetics of the electronic changes occurring at Pt during potential cycling. This technique is not only complementary to $\Delta\mu$ XANES but also represents a decisive step toward establishing practical design principles for catalyst optimization. By linking transient structural changes to electrochemical behavior, FEXRAV bridges the gap between fundamental spectroscopic observation and operational catalyst design. Specifically, it enables the identification of operating potentials that minimize site blocking, supports the rational design of Pt alloys with improved tolerance to to contamination by phosphorus-containing species, and guides strategies to mitigate performance losses in HT-PEMFCs.

In turn, the $\Delta\mu$ XANES method isolates surface-specific spectral changes while the nanoparticle core remains largely unaffected. However, this technique can only be reliably applied to catalyst systems where core stability is ensured, as any bulk restructuring would compromise its surface sensitivity. Under such conditions, $\Delta\mu$ XANES becomes particularly powerful for investigating the competition of different adsorbates for active sites. While FEXRAV identifies when rapid electronic changes occur during the electrochemical process, $\Delta\mu$ XANES identifies the surface species responsible for these changes under well-defined electrochemical conditions. The combination of both techniques therefore enables direct correlation between dynamic electronic response and surface speciation, providing mechanistic insight that cannot be obtained from either technique alone.

Finally, the machine learning model, trained on both Pt/C and Pt alloy datasets, validates the robustness of the combined spectroscopic approach and underscores its predictive capability across a broader class of catalysts. By reducing the reliance on extensive trial-and-error experimentation and costly synchrotron campaigns, ML-assisted XAS analysis significantly accelerates the discovery and optimization of new electrocatalysts and shows promise for extension to non-noble metal catalyst systems.

Overall, this work establishes a clear methodological advance beyond qualitative operando spectroscopy by demonstrating that the combination of $\Delta\mu$ XANES and FEXRAV provides complementary access to steady-state surface speciation and transient electronic structure dynamics during competitive adsorption. Rather than measuring the same quantity, the two techniques probe different but directly related aspects of the catalyst surface, allowing the dynamic electronic response observed by FEXRAV to be interpreted in terms of the underlying adsorbate population identified by $\Delta\mu$ XANES. The ability to simultaneously resolve surface composition, transient electronic changes, and predictive spectral trends represents a significant step toward a comprehensive operando description of electrocatalytic interfaces. Beyond the methodological advance, the combined analysis provides new insight into the poisoning mechanism of phosphorus-containing impurities on Pt, suggesting that H_3PO_3 exhibits a preferential affinity

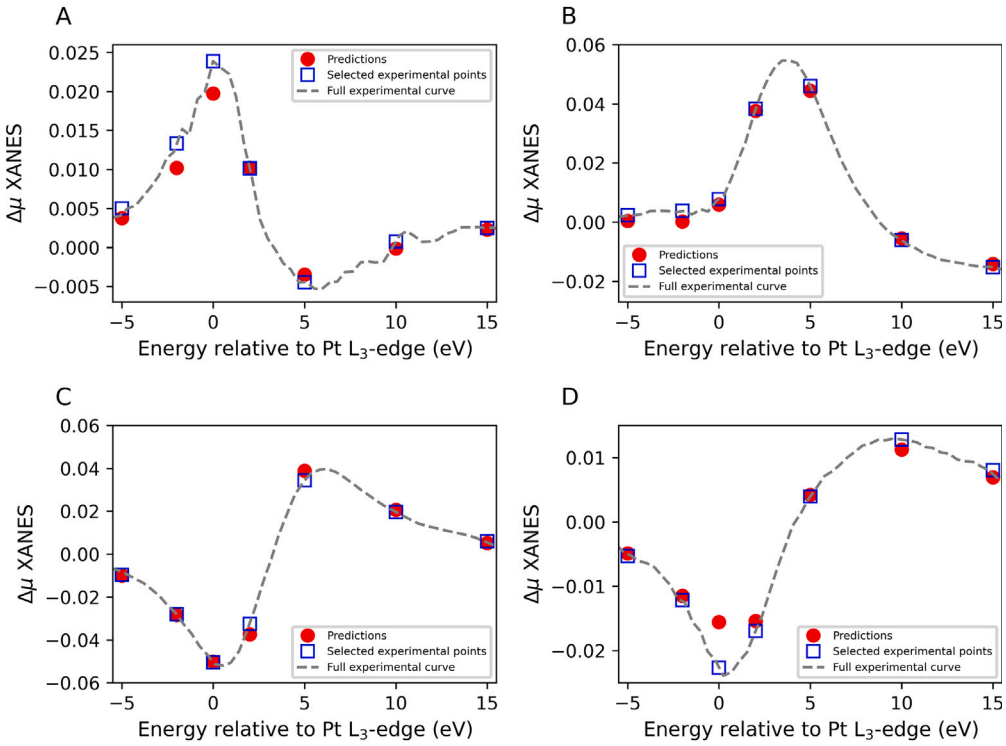


Fig. 5. Comparison between the experimental (blue squares) and predicted (red circles) points of the XANES spectra of four experiments (subplots A to D) selected from the test set. The full experimental curve (dashed gray line) is also shown for guiding the eyes.

for low-coordination Pt sites, commonly associated with (100)/(110)-like domains and surface defects. Such preferential adsorption not only competes directly with CO for adsorption sites but may also suppress the formation of oxygenated Pt species at these reactive sites, thereby modifying the interfacial reaction pathways involved in CO oxidation.

In the context of HT-PEMFCs, these findings provide a basis for understanding how H_3PO_3 contamination modifies Pt surface availability and the formation of oxygenated surface species, linking site-specific competitive adsorption to the altered interfacial processes underlying catalyst poisoning. These findings establish a mechanistic framework for interpreting phosphorus poisoning under HT-PEMFC operating conditions and provide a basis for the rational development of more poison-tolerant Pt electrocatalysts.

4. Experimental

4.1. Chemicals

Phosphoric acid crystals (99.999% purity for trace metals, product number 310271), isopropyl alcohol (ACS grade, product number 59300), and phosphorous acid crystals (99% purity for trace metals, product number 215112) were sourced from Merck. A 5 wt% Nafion solution, was acquired from Quintech (product number 13102). Pt nanoparticles supported on Vulcan XC-72 were used (40 wt%, Pt/C, HiSPEC 4000 by Johnson Matthey). Deionized water used in the experiments was of an ultra-high purity grade, with a resistivity of 18.18 MΩ cm. Gas diffusion layers (GDL) for the gas diffusion electrodes (GDE) were the Sigracet 38 BB from SGL Carbon.

4.2. Electrode preparation – Gas diffusion electrode

The working electrodes, WE, were prepared as gas diffusion electrodes (GDE) using the spray coating method. The ink composition included 500 mg of Pt/C (Pt loading 20 wt%), 500 mg of Nafion solution (5 wt%), and 16 mL of isopropanol. The ink underwent sonication for 30 min in an ice bath to ensure thorough mixing and homogeneity before use. This ink was then deposited onto the gas diffusion layer (5 × 5 cm^2). The final catalyst loading was 1 mg_{Pt} cm^{-2}.

4.3. In-situ cell

A half-cell was adapted for in-situ XAS measurements during electrochemical experiments (Fig. 6). The cell consists of a PTFE body with a capacity for 100 mL of electrolyte. A window at the back of the working electrode (GDE) is sealed with Kapton (DuPont) tape to prevent leaks. This cell is used in fluorescence mode. It is important to note that in-situ measurements by transmittance require more adaptations to the electrochemical cells, as the presence of bubbles and electrolyte can directly affect the beam path, thereby hindering signal detection. Therefore, we chose a more robust cell, specifically adapted for fluorescence measurements. The setup includes a working electrode (GDE), a reference electrode (Ag/AgCl KCl saturated), and a counter electrode (Pt mesh). This arrangement facilitates controlled electrochemical reactions while concurrently allowing for the examination of samples under a synchrotron beam (fluorescence mode). All experiments were carried out at 25 °C.

4.4. XAS measurements

4.4.1. EXAFS fit

The XAS measurements were performed at the beamline P65 at DESY (Hamburg). EXAFS (Extended X-ray Absorption Fine Structure) spectra normalization was performed using the range of 150 to 950 eV above the absorption edge with the aid of Bessy software. Post-normalization, the spectrum was processed using the SimXLite software for EXAFS fits. Scattering paths were constructed using the FEFF8.4 software. The primary shells considered were Pt–Pt and Pt–O. The energy alignment was performed considering the Pt foil as reference. The parameter S_0^2 used was 0.95. To simplify the fitting process, the Debye–Waller factor values, $2\sigma^2$, were standardized at 0.002 $Å^2$ for

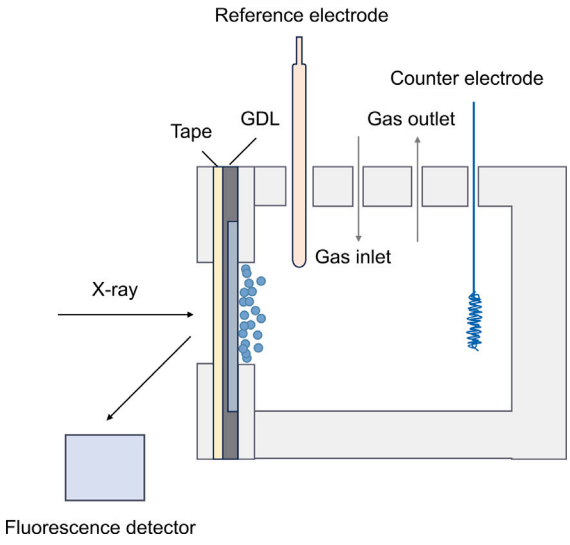


Fig. 6. In-situ EC-XAS electrochemical half-cell.

Pt−O, while for Pt−Pt, these values were adjusted freely. Fittings were executed in k space, within the ranges Δk = [2.0 − 15.8] $Å^{-1}$ and ΔR = [1.0−3.5] Å. The fit parameters, including bond distance and coordination number, exhibited an error margin of approximately 10%. The R-factor was always smaller than 10.

4.4.2. $\Delta\mu$ XANES

The $\Delta\mu$ XANES approach was utilized to assess the information about the species adsorbed on Pt. This involved calculating the absorption coefficient, μ, using Bessy software, followed by normalization of the data. To align the normalized data, a Pt foil was used as the benchmark. The $\Delta\mu$ values were determined by deducting the baseline measurement at 0.5 V_{RHE}, double layer region, in 1 mol L^{-1} H_3PO_4, from $\mu_{E,[H_3PO_3]}$(adsorbate/Pt), recorded under various electrolyte composition and potentials, as outlined in Eq. (1), which is a common practice in similar half-cell studies [4,5,59]. The $\Delta\mu$ XANES analysis covered an energy range from −20 to 30 eV, relative to the Pt L_3−edge at 11,564 eV.

$$\Delta\mu_{E,[H_3PO_3]} = \mu_{E,[H_3PO_3]}(\text{adsorbate/Pt}) - \mu_{0.5V_{RHE},[H_3PO_4]=1\ \text{mol}\ L^{-1}}(\text{double layer}) \quad (1)$$

4.4.3. Machine learning

A ML model was trained using six experimental parameters used to prepare and test the electrodes: [H_3PO_3], applied potential (E vs. RHE), gas (N_2 or CO), [H_3PO_4], [$HClO_4$], and catalyst (Pt on vulcan carbon, PtCo on vulcan carbon, and PtCo_rGo). The trained model predicted $\Delta\mu$ XANES at seven different energy values (in eV) relative to the Pt L_3 edge: −5, −2, 0, 2, 5, 10, and 15, arbitrarily chosen to describe the experimental spectra. The dataset comprised of 76 experiments and six features. An initial screening of different models was performed, from where Random Forests (RF) was chosen due to its better performance. The dataset was shuffled and split into training (60 samples or ca 80%) and test (16 samples) sets using a random seed of 42. Hyperparameters like the number of estimators or depth of the tree were not optimized due to the very small size of the dataset, so that default values (e.g., 100 estimators, no maximum depth of tree, split criterion = 'gini') were used. After training the RF model with the training set, predictions of $\Delta\mu$ XANES were performed on the test set to evaluate the generalizability of the model, as well as on the training set to analyze overfitting. The model variance was investigated by splitting the dataset using 100 different random seeds and averaging the Mean Absolute Error (*MAE*) and the coefficient of determination, R^2. The code for the ML model was written in Python 3 and standard Python packages were used (e.g., scikit-learn, pandas, numpy). General results about predictions, training errors and variance analysis, as well as the link to access the code are shown in the SI.

4.4.4. Single edge energy (FEXRAV)

Fixed-Energy X-ray Absorption Voltammetry (FEXRAV) was employed to obtain time-resolved, element-specific information during the electrochemical measurements. The methodology consisted of three main steps, summarized in Fig. 1. First, conventional XANES spectra were collected under representative electrochemical conditions to identify an excitation energy sensitive to changes in the Pt electronic structure. The fixed excitation energy was selected within the white-line region based on the largest fluorescence-intensity variation between the investigated states. An excitation energy of 11,568 eV at the Pt L_3-edge, approximately 5 eV above the white-line maximum, was selected for the FEXRAV measurements. The fluorescence intensity at this fixed energy was then continuously recorded during potential cycling and normalized by the incident X-ray intensity (I_0).

Synchronization: The fluorescence signal at 11,568 eV was acquired at approximately 3 points per second, corresponding to a temporal resolution of approximately 0.33 s per point and, at a scan rate of 20 mV s^{-1}, a potential resolution of approximately 6.67 mV per acquired point. Since the potentiostat was not directly integrated with the spectrometer acquisition system, the electrochemical and fluorescence data were synchronized during post-processing. The fluorescence sequences were temporally aligned using the reproducible fluorescence change observed at 0.1 V vs. RHE as a common reference point (Figure S6). Following temporal alignment, the potential-versus-time data recorded by the potentiostat were interpolated onto the fluorescence time series, allowing each fluorescence measurement to be assigned to its corresponding electrode potential. The aligned fluorescence data were subsequently differentiated with respect to time to obtain $\frac{dFluo}{dt}$, which was plotted as a function of the corresponding interpolated electrode potential. This treatment highlights potential regions associated with rapid changes in the Pt L_3-edge fluorescence response, providing a transient Pt-specific electronic response that can be correlated with features observed in the electrochemical data.

Synchronization uncertainty: The uncertainty associated with the temporal alignment procedure was estimated by determining the position of a representative fluorescence maximum using three independent approaches: (i) visual inspection, (ii) selection of the highest sampled point, and (iii) Origin Peak Analyzer. Based on the spread between these methods, the alignment uncertainty was estimated to be approximately ±3.3 mV. Even under the conservative assumption of a full acquisition interval, this alignment uncertainty would increase to ±6.7 mV at a scan rate of 20 mV s^{-1}.

4.4.5. Electrochemical measurements

Electrochemical measurements were conducted using the Biologic potentiostat (model SP-300). The electrolyte employed was 1 mol L^{-1} H_3PO_4, which is a doping agent in membranes used in HT−PEM fuel cells. A volume of 100 mL of this electrolyte was utilized for all electrochemical measurements. The gas flow was regulated using mass flow controllers (Bronkhorst).

4.4.6. EC-XAS in-situ measurements

The electrochemical measurements were conducted in three steps:

Step 1: $\Delta\mu$ XANES — Chronoamperometric measurements were carried out at different potentials (from 0.1 to 1 V_{RHE}), during which XAS spectra (Pt L_3−edge, 3 scans) were acquired. This step was crucial for obtaining spectra at different potentials, later used to derive $\Delta\mu$ XANES features. A potential of 0.5 V_{RHE} in the electrolyte without any additives (1 mol L^{-1} H_3PO_4) served as the reference spectrum for $\Delta\mu$ XANES acquisition.

Step 2: This stage focused on the adsorption and removal of CO from the Pt surface in both the absence and presence of H_3PO_3 at various concentrations (0, 2×10^{-6}, 1×10^{-5}, 2×10^{-5}, 1×10^{-4}, 2×10^{-4} mol L^{-1}). H_3PO_3 aliquots were directly added to the electrochemical cell and the following steps were followed:

- XAS with CO adsorbed: A potential of 0.1 V_{RHE} was applied during the electrolyte saturation with CO (30 mL min^{-1}). After 10 min, while still bubbling CO and under a constant potential of 0.1 V_{RHE}, 3 spectra were acquired. The goal here was to obtain the $\Delta\mu$ XANES feature for CO as an adsorbate.
- Removal of excess CO: Excess CO in the solution was removed using N_2 bubbling (20 min, 300 mL min^{-1}) while maintaining a constant potential of 0.1 V_{RHE}. This step is essential to remove CO dissolved in the electrolyte.
- FEXRAV measurement: CO stripping was synchronized with XAS measurements using the fixed energy method. Here, a specific energy, in this case 11,568 eV, was selected, and the XAS signal intensity was measured concurrently with cyclic voltammetry. During this process, the solution was continuously flushed with N_2. Two CV cycles were measured at 20 mV s^{-1} from 0.1 to 1.0 V_{RHE}.
- The preceding steps were repeated for each concentration of H_3PO_3.

Step 3: $\Delta\mu$ XANES — After CO removal, XAS spectra were obtained for 3 different potentials (0.1 V_{RHE} for hydrogen adsorption region, 0.5 V_{RHE} for the double layer region, and 1 V_{RHE} for the Pt–O region). This stage was key to tracking changes in various $\Delta\mu$ XANES features and thereby understanding the competition of H_3PO_3 for active sites on Pt at different potential ranges.

4.4.7. FEFF 8.4 calculations

The $\Delta\mu$ XANES profiles were generated through simulations using the FEFF 8.4 software. These calculations involved both a Pt_6 Janin cluster in its basic form and the same cluster with added adsorbates. We derived the differential spectra by comparing the simulated μ values in a similar manner to the processing of experimental difference spectra (Eq. (2)). The simulations focused on the adsorbed reaction intermediate species that are most commonly encountered during operation of HT-PEM cells, namely H, O, CO, and H_3PO_3. In an effort to streamline the simulation process, the H_3PO_3 molecule was represented as PO_3. During the FEFF8.4 simulation process, emphasis was placed on a single predominant atom, as combining contributions from various Pt atoms in the cluster showed negligible impact on the final simulated signatures. The expected $\Delta\mu$ signatures for surfaces containing different adsorbates were obtained by linear combinations of the theoretical $\Delta\mu$ features generated from the FEFF calculations (Figure S13).

$$\Delta\mu_{species} = \mu_{species}(\text{adsorbate/Pt}_6) - \mu_{clean}(\text{clean Pt}_6) \quad (2)$$

CRediT authorship contribution statement

Bruna Ferreira Gomes: Writing – review & editing, Writing – original draft, Visualization, Validation, Resources, Project administration, Methodology, Investigation, Formal analysis, Data curation, Conceptualization. **Rameshwori Loukrakpam:** Writing – review & editing, Writing – original draft, Visualization, Supervision, Methodology, Investigation, Conceptualization. **Carlos M.S. Lobo:** Writing – review & editing, Writing – original draft, Methodology, Investigation, Formal analysis, Data curation. **Tomas Bystron:** Writing – review & editing, Writing – original draft, Visualization, Resources, Methodology, Investigation, Funding acquisition, Data curation. **Martin Prokop:** Writing – review & editing, Writing – original draft, Visualization, Validation, Methodology, Investigation, Funding acquisition, Data curation, Conceptualization. **Rodrigo Q. Albuquerque:** Writing – review & editing, Writing – original draft, Visualization, Validation, Methodology, Investigation, Data curation. **Lu Xia:** Writing – review & editing, Writing – original draft, Visualization, Validation, Formal analysis. **Wulyu Jiang:** Writing – review & editing, Writing – original draft, Visualization, Validation, Formal analysis. **F. Pelayo García de Arquer:** Writing – review & editing, Supervision, Resources, Funding acquisition. **Karel Bouzek:** Writing – review & editing, Visualization, Supervision, Resources, Funding acquisition, Conceptualization. **Christina Roth:** Writing – review & editing, Visualization, Supervision, Resources, Project administration, Funding acquisition, Conceptualization.

Declaration of competing interest

The authors declare that they have no known competing financial interests or personal relationships that could have appeared to influence the work reported in this paper.

Acknowledgments

The authors acknowledge DESY (Hamburg, Germany), a member of the Helmholtz Association HGF, for the provision of experimental facilities. Parts of this research were carried out at PETRA III and we would like to thank Edmund Welter for assistance in using the P65 beamline. Beamtime was allocated for proposals I-20211432 and I-20221072. This work is funded by the Federal Ministry of Research, Technology, and Space (BMFTR) under the funding codes Live XAS (Grant 05K22WC1) and HighHy (Grant 03SF0689B). This study was additionally supported by the Deutsche Forschungsgemeinschaft (DFG, German Research Foundation) Collaborative Research Center 1585 (A02-492723217).

The authors would like to express their gratitude to Dr. Michael Haumann and Prof. Holger Dau from Freie Universität Berlin for their invaluable assistance in the evaluation of XAS data and for providing access to the SimXLite software (for EXAFS fit) developed by the scientists at the KMC-3 beamline at BESSY-HZB. We gratefully acknowledge Nicolò Orsingher for the insightful discussions regarding the interpretation of the FEXRAV data, which significantly improved our understanding of the results. We sincerely thank Laís Gimenes Vernasqui for her insightful discussions and contributions to the deconvolution analysis.

Funding support was also provided by the Czech Science Foundation (GACR) under Project No. 22-23668 K. Additionally, support was given by the project "The Energy Conversion and Storage", funded as project No. CZ.02.01.01/00/22_008/0004617 by Programme Johannes Amos Comenius, call Excellent Research. ICFO team acknowledges support from CEX2019-000910-S (MCIN/AEI/10.13039/501100011033), Fundació Cellex, Fundació Mir-Puig, PID2022-138127NA-I00 funded by MCIN/AEI/10.13039/501100011033, the European Union (NASCENT, 101077243), and the European Union's Horizon Europe research and innovation programme under the Marie Skłodowska-Curie grant agreement No. 101150688.

Appendix A. Supplementary data

The supporting information PDF is provided free of charge with this publication. It contains the experimental details, further information about the FEXRAV and $\Delta\mu$ XANES methods and information about the machine learning procedures and EXAFS fits.

Supplementary material related to this article can be found online at https://doi.org/10.1016/j.surfin.2026.110279.

Data availability

Data will be made available on request.

References

[1] J. Wang, H.-Y. Tan, M.-Y. Qi, J.-Y. Li, Z.-R. Tang, N.-T. Suen, Y.-J. Xu, H.M. Chen, Spatially and temporally understanding dynamic solid–electrolyte interfaces in carbon dioxide electroreduction, Chem. Soc. Rev. 52 (2023) 5013–5050, http://dx.doi.org/10.1039/D2CS00441K.

[2] D. Bohra, J.H. Chaudhry, T. Burdyny, E.A. Pidko, W.A. Smith, Modeling the electrical double layer to understand the reaction environment in a CO_2 electrocatalytic system, Energy Env. Sci. 12 (2019) 3380–3389, http://dx.doi.org/10.1039/C9EE02485A.

[3] C.-S. Hsu, J. Wang, Y.-C. Chu, J.-H. Chen, C.-Y. Chien, K.-H. Lin, L.D. Tsai, H.-C. Chen, Y.-F. Liao, N. Hiraoka, Y.-C. Cheng, H.M. Chen, Activating dynamic atomic-configuration for single-site electrocatalyst in electrochemical CO_2 reduction, Nat. Commun. 14 (2023) 5245, http://dx.doi.org/10.1038/s41467-023-40970-y.

[4] D.E. Ramaker, D.C. Koningsberger, The atomic AXAFS and 4μ XANES techniques as applied to heterogeneous catalysis and electrocatalysis, Phys. Chem. Chem. Phys. 12 (2010) 5514–5534, http://dx.doi.org/10.1039/B927120C.

[5] B.F. Gomes, M. Prokop, T. Bystron, R. Loukrakpam, J. Melke, C.M.S. Lobo, M. Fink, M. Zhu, E. Voloshina, M. Kutter, H. Hoffmann, K.V. Yusenko, A.G. Buzanich, B. Röder, K. Bouzek, B. Paulus, C. Roth, Following adsorbed intermediates on a platinum gas diffusion electrode in H_3PO_3-containing electrolytes using in situ X-ray absorption spectroscopy, ACS Catal. 12 (18) (2022) 11472–11484, http://dx.doi.org/10.1021/acscatal.2c02630.

[6] M. Newville, Fundamentals of XAFS, Rev. Miner. Geochem. 78 (1) (2014) 33–74, http://dx.doi.org/10.2138/rmg.2014.78.2.

[7] J.J. Rehr, R.C. Albers, Theoretical approaches to x-ray absorption fine structure, Rev. Modern Phys. 72 (3) (2000) 621–654, http://dx.doi.org/10.1103/RevModPhys.72.621, RMP.

[8] M. Wang, L. Árnadóttir, Z.J. Xu, Z. Feng, In situ X-ray absorption spectroscopy studies of nanoscale electrocatalysts, Nano-Micro Lett. 11 (1) (2019) 47, http://dx.doi.org/10.1007/s40820-019-0277-x.

[9] J. Timoshenko, B. Roldan Cuenya, In situ/operando electrocatalyst characterization by X-ray absorption spectroscopy, Chem. Rev. 121 (2) (2021) 882–961, http://dx.doi.org/10.1021/acs.chemrev.0c00396.

[10] M.F. Tesch, S.A. Bonke, R. Golnak, J. Xiao, A.N. Simonov, R. Schlögl, Vacuum compatible flow-cell for high-quality in situ and operando soft X-ray photon-in–photon-out spectroelectrochemical studies of energy materials, Electrochem. Sci. Adv. 2 (6) (2022) e2100141, http://dx.doi.org/10.1002/elsa.202100141.

[11] A.I. Frenkel, Applications of extended X-ray absorption fine-structure spectroscopy to studies of bimetallic nanoparticle catalysts, Chem. Soc. Rev. 41 (24) (2012) 8163–8178, http://dx.doi.org/10.1039/C2CS35174A.

[12] A. Kuzmin, J. Chaboy, EXAFS and XANES analysis of oxides at the nanoscale, IUCrJ 1 (6) (2014) 571–589, http://dx.doi.org/10.1107/S2052252514021101.

[13] A.E. Russell, A. Rose, X-ray absorption spectroscopy of low temperature fuel cell catalysts, Chem. Rev. 104 (10) (2004) 4613–4636, http://dx.doi.org/10.1021/cr020708r.

[14] Q. Jia, E. Liu, L. Jiao, S. Pann, S. Mukerjee, X-Ray absorption spectroscopy characterizations on PGM-Free electrocatalysts: Justification, advantages, and limitations, Adv. Mater. 31 (31) (2019) 1805157, http://dx.doi.org/10.1002/adma.201805157.

[15] A. Bergmann, T.E. Jones, E. Martinez Moreno, D. Teschner, P. Chernev, M. Gliech, T. Reier, H. Dau, P. Strasser, Unified structural motifs of the catalytically active state of Co(oxyhydr)oxides during the electrochemical oxygen evolution reaction, Nat. Catal. 1 (9) (2018) 711–719, http://dx.doi.org/10.1038/s41929-018-0141-2.

[16] A. Eilert, F.S. Roberts, D. Friebel, A. Nilsson, Formation of copper catalysts for CO_2 reduction with high ethylene/methane product ratio investigated with in situ X-ray absorption spectroscopy, J. Phys. Chem. Lett. 7 (8) (2016) 1466–1470, http://dx.doi.org/10.1021/acs.jpclett.6b00367.

[17] D. Gashnikova, F. Maurer, M.R. Bauer, S. Bernart, J. Jelic, M. Lützen, C.B. Maliakkal, P. Dolcet, F. Studt, C. Kübel, C.D. Damsgaard, M. Casapu, J.-D. Grunwaldt, Lifecycle of Pd clusters: Following the formation and evolution of active Pd clusters on ceria during CO oxidation by in situ/operando characterization techniques, ACS Catal. 14 (19) (2024) 14871–14886, http://dx.doi.org/10.1021/acscatal.4c02077.

[18] O. Mathon, I. Kantor, S. Pascarelli, Time-resolved XAS using an energy dispersive spectrometer: Techniques and applications, in: X-Ray Absorption and X-Ray Emission Spectroscopy, Wiley Online Books, 2016, pp. 185–212, http://dx.doi.org/10.1002/9781118844243.ch8.

[19] J.G. Moya-Cancino, A.-P. Honkanen, A.M.J. van der Eerden, H. Schaink, L. Folkertsma, M. Ghiasi, A. Longo, F.M.F. de Groot, F. Meirer, S. Huotari, B.M. Weckhuysen, In-situ X-Ray absorption near edge structure spectroscopy of a solid catalyst using a laboratory-based set-up, ChemCatChem 11 (3) (2019) 1039–1044, http://dx.doi.org/10.1002/cctc.201801822.

[20] A.E. Russell, S. Maniguet, R.J. Mathew, J. Yao, M.A. Roberts, D. Thompsett, In situ X-ray absorption spectroscopy and X-ray diffraction of fuel cell electrocatalysts, J. Power Sources 96 (1) (2001) 226–232, http://dx.doi.org/10.1016/S0378-7753(01)00573-0.

[21] J.A. van Bokhoven, C. Louis, J.T. Miller, M. Tromp, O.V. Safonova, P. Glatzel, Activation of oxygen on gold/alumina catalysts: In situ high-energy-resolution fluorescence and time-resolved X-ray spectroscopy, Angew. Chem. Int. Ed. 45 (28) (2006) 4651–4654, http://dx.doi.org/10.1002/anie.200601184.

[22] E.A. Carbonio, J.-J. Velasco-Velez, R. Schlögl, A. Knop-Gericke, Perspective—Outlook on operando photoelectron and absorption spectroscopy to probe catalysts at the solid-liquid electrochemical interface, J. Electrochem. Soc. 167 (5) (2020) 054509, http://dx.doi.org/10.1149/1945-7111/ab68d2.

[23] P. Ghigna, E. Quartarone, Operando x-ray absorption spectroscopy on battery materials: a review of recent developments, J. Phys.: Energy 3 (3) (2021) 032006, http://dx.doi.org/10.1088/2515-7655/abf2db.

[24] B. Lassalle-Kaiser, S. Gul, J. Kern, V.K. Yachandra, J. Yano, In situ/operando studies of electrocatalysts using hard X-ray spectroscopy, J. Electron Spectrosc. Relat. Phenom. 221 (2017) 18–27, http://dx.doi.org/10.1016/j.elspec.2017.05.001.

[25] M. Tada, T. Uruga, Y. Iwasawa, Key factors affecting the performance and durability of cathode electrocatalysts in polymer electrolyte fuel cells characterized by in situ real time and spatially resolved XAFS techniques, Catal. Lett. 145 (1) (2015) 58–70, http://dx.doi.org/10.1007/s10562-014-1428-9.

[26] C.H.M. van Oversteeg, H.Q. Doan, F.M.F. de Groot, T. Cuk, In situ X-ray absorption spectroscopy of transition metal based water oxidation catalysts, Chem. Soc. Rev. 46 (1) (2017) 102–125, http://dx.doi.org/10.1039/C6CS00230G.

[27] C. Sherwin, V. Celorrio, U. Podbevsek, K. Rigg, T. Hodges, A. Ibraliu, A.J. Telfer, L. McLeod, A. Difilippo, E.C. Corbos, C. Zalitis, A.E. Russell, An optimised cell for in situ XAS of gas diffusion electrocatalyst electrodes, ChemCatChem 16 (19) (2024) e202400221, http://dx.doi.org/10.1002/cctc.202400221.

[28] L. Ostervold, A.S. Hoffman, D. Thompson, S.R. Bare, E.L. Clark, A versatile electrochemical cell for operando XAS, ChemCatChem 16 (15) (2024) e202400072, http://dx.doi.org/10.1002/cctc.202400072.

[29] M. Wang, J. Zhang, S. Favero, L.J.R. Higgins, H. Luo, I.E.L. Stephens, M.-M. Titirici, Resolving optimal ionomer interaction in fuel cell electrodes via operando X-ray absorption spectroscopy, Nat. Commun. 15 (1) (2024) 9390, http://dx.doi.org/10.1038/s41467-024-53823-z.

[30] M.F. Tesch, A.N. Simonov, Tracking the transient: Real-time exploration of electromaterials by dynamic single energy X-ray spectroelectrochemistry, Curr. Opin. Electrochem. 35 (2022) 101038, http://dx.doi.org/10.1016/j.coelec.2022.101038.

[31] B. Bornmann, J. Kläs, O. Müller, D. Lützenkirchen-Hecht, R. Frahm, The quick EXAFS setup at beamline P64 at PETRA III for up to 200 spectra per second, AIP Conf. Proc. 2054 (1) (2019) 040008, http://dx.doi.org/10.1063/1.5084609.

[32] A.H. Clark, P. Steiger, B. Bornmann, S. Hitz, R. Frahm, D. Ferri, M. Nachtegaal, Fluorescence-detected quick-scanning X-ray absorption spectroscopy, J. Synchrotron Radiat. 27 (3) (2020) 681–688, http://dx.doi.org/10.1107/S1600577520002350.

[33] N. Ishiguro, T. Saida, T. Uruga, S.-i. Nagamatsu, O. Sekizawa, K. Nitta, T. Yamamoto, S.-i. Ohkoshi, Y. Iwasawa, T. Yokoyama, M. Tada, Operando time-resolved X-ray absorption fine structure study for surface events on a Pt3Co/C cathode catalyst in a polymer electrolyte fuel cell during voltage-operating processes, ACS Catal. 2 (7) (2012) 1319–1330, http://dx.doi.org/10.1021/cs300228p.

[34] J. McBreen, W.E. O'Grady, G. Tourillon, E. Dartyge, A. Fontaine, K.I. Pandya, In situ time-resolved x-ray absorption near edge structure study of the nickel oxide electrode, J. Phys. Chem. 93 (17) (1989) 6308–6311, http://dx.doi.org/10.1021/j100354a010.

[35] P.G. Allen, S.D. Conradson, M.S. Wilson, S. Gottesfeld, I.D. Raistrick, J. Valerio, M. Lovato, In situ structural characterization of a platinum electrocatalyst by dispersive x-ray absorption spectroscopy, Electrochim. Acta 39 (16) (1994) 2415–2418, http://dx.doi.org/10.1016/0013-4686(94)E0196-U.

[36] M. Tada, S. Murata, T. Asakoka, K. Hiroshima, K. Okumura, H. Tanida, T. Uruga, H. Nakanishi, S.-i. Matsumoto, Y. Inada, M. Nomura, Y. Iwasawa, In situ time-resolved dynamic surface events on the Pt/C cathode in a fuel cell under operando conditions, Angew. Chem. Int. Ed. 46 (23) (2007) 4310–4315, http://dx.doi.org/10.1002/anie.200604732.

[37] H. Imai, K. Izumi, M. Matsumoto, Y. Kubo, K. Kato, Y. Imai, In situ and real-time monitoring of oxide growth in a few monolayers at surfaces of platinum nanoparticles in aqueous media, J. Am. Chem. Soc. 131 (17) (2009) 6293–6300, http://dx.doi.org/10.1021/ja810036h.

[38] A. Filipponi, M. Borowski, P.W. Loeffen, S.D. Panfilis, A.D. Cicco, F. Sperandini, M. Minicucci, M. Giorgetti, Single-energy x-ray absorption detection: a combined electronic and structural local probe for phase transitions in condensed matter, J. Phys.: Condens. Matter. 10 (1) (1998) 235, http://dx.doi.org/10.1088/0953-8984/10/1/026.

[39] A. Minguzzi, O. Lugaresi, C. Locatelli, S. Rondinini, F. D'Acapito, E. Achilli, P. Ghigna, Fixed energy X-ray absorption voltammetry, Anal. Chem. 85 (15) (2013) 7009–7013, http://dx.doi.org/10.1021/ac401414v.

[40] J. Wang, C.-S. Hsu, T.-S. Wu, T.-S. Chan, N.-T. Suen, J.-F. Lee, H.M. Chen, In situ X-ray spectroscopies beyond conventional X-ray absorption spectroscopy on deciphering dynamic configuration of electrocatalysts, Nat. Commun. 14 (2023) 6576, http://dx.doi.org/10.1038/s41467-023-42370-8.

[41] S. Rondinini, O. Lugaresi, E. Achilli, C. Locatelli, A. Minguzzi, A. Vertova, P. Ghigna, C. Comninellis, Fixed energy X-ray absorption voltammetry and extended X-ray absorption fine structure of ag nanoparticle electrodes, J. Electroanal. Chem. 766 (2016) 71–77, http://dx.doi.org/10.1016/j.jelechem.2016.01.039.

[42] T. Baran, S. Wojtyła, C. Lenardi, A. Vertova, P. Ghigna, E. Achilli, M. Fracchia, S. Rondinini, A. Minguzzi, An efficient cuxo photocathode for hydrogen production at neutral pH: New insights from combined spectroscopy and electrochemistry, ACS Appl. Mater. & Interfaces 8 (33) (2016) 21250–21260, http://dx.doi.org/10.1021/acsami.6b03345.

[43] G. Montegrossi, A. Giaccherini, E. Berretti, F.D. Benedetto, M. Innocenti, F. d'Acapito, A. Lavacchi, Computational speciation models: A tool for the interpretation of spectroelectrochemistry for catalytic layers under operative conditions, J. Electrochem. Soc. 164 (11) (2017) E3690, http://dx.doi.org/10.1149/2.0711711jes.

[44] M.R. Mohammadi, S. Loos, P. Chernev, C. Pasquini, I. Zaharieva, D. González-Flores, P. Kubella, K. Klingan, R.D.L. Smith, H. Dau, Exploring the limits of self-repair in cobalt oxide films for electrocatalytic water oxidation, ACS Catal. 10 (14) (2020) 7990–7999, http://dx.doi.org/10.1021/acscatal.0c01944.

[45] R.D.L. Smith, C. Pasquini, S. Loos, P. Chernev, K. Klingan, P. Kubella, M.R. Mohammadi, D. Gonzalez-Flores, H. Dau, Spectroscopic identification of active sites for the oxygen evolution reaction on iron-cobalt oxides, Nat. Commun. 8 (1) (2017) 2022, http://dx.doi.org/10.1038/s41467-017-01949-8.

[46] D. González-Flores, K. Klingan, P. Chernev, S. Loos, M.R. Mohammadi, C. Pasquini, P. Kubella, I. Zaharieva, R.D.L. Smith, H. Dau, Nickel-iron catalysts for electrochemical water oxidation – redox synergism investigated by in situ X-ray spectroscopy with millisecond time resolution, Sustain. Energy & Fuels 2 (9) (2018) 1986–1994, http://dx.doi.org/10.1039/C8SE00114F.

[47] J. Meng, Z. Cui, X. Yang, S. Zhu, Z. Li, K. Qi, L. Zheng, Y. Liang, Cobalt-iron (oxides) water oxidation catalysts: Tracking catalyst redox states and reaction dynamic mechanism, J. Catalysis 365 (2018) 227–237, http://dx.doi.org/10.1016/j.jcat.2018.06.031.

[48] M. Fracchia, A. Visibile, E. Ahlberg, A. Vertova, A. Minguzzi, P. Ghigna, S. Rondinini, α- and γ-FeOOH: Stability, reversibility, and nature of the active phase under hydrogen evolution, ACS Appl. Energy Mater. 1 (4) (2018) 1716–1725, http://dx.doi.org/10.1021/acsaem.8b00209.

[49] M. Fracchia, V. Cristino, A. Vertova, S. Rondinini, S. Caramori, P. Ghigna, A. Minguzzi, Operando X-ray absorption spectroscopy of WO3 photoanodes, Electrochim. Acta 320 (2019) 134561, http://dx.doi.org/10.1016/j.electacta.2019.134561.

[50] E. Berretti, A. Giaccherini, G. Montegrossi, F. D'Acapito, F. Di Benedetto, C. Zafferoni, A. Puri, G.O. Lepore, H. Miller, W. Giurlani, M. Innocenti, F. Vizza, A. Lavacchi, In-situ quantification of nanoparticles oxidation: A fixed energy X-ray absorption approach, Catalysts 9 (8) (2019) 659, http://dx.doi.org/10.3390/catal9080659.

[51] T. Ishihara, T. Tokushima, Y. Horikawa, M. Kato, I. Yagi, Development of a spectro-electrochemical cell for soft X-ray photon-in photon-out spectroscopy, Rev. Sci. Instrum. 88 (10) (2017) 104101, http://dx.doi.org/10.1063/1.4997820.

[52] D. Drevon, M. Görlin, P. Chernev, L. Xi, H. Dau, K.M. Lange, Uncovering the role of oxygen in Ni-Fe(OxHy) electrocatalysts using in situ soft X-ray absorption spectroscopy during the oxygen evolution reaction, Sci. Rep. 9 (1) (2019) 1532, http://dx.doi.org/10.1038/s41598-018-37307-x.

[53] C. Schwanke, L. Xi, K.M. Lange, A soft XAS transmission cell for operando studies, J. Synchrotron Radiat. 23 (6) (2016) 1390–1394, http://dx.doi.org/10.1107/S1600577516014697.

[54] L.J. Falling, R.V. Mom, L.E. Sandoval Diaz, S. Nakhaie, E. Stotz, D. Ivanov, M. Hävecker, T. Lunkenbein, A. Knop-Gericke, R. Schlögl, J.-J. Velasco-Vélez, Graphene-capped liquid thin films for electrochemical operando X-ray spectroscopy and scanning electron microscopy, ACS Appl. Mater. & Interfaces 12 (33) (2020) 37680–37692, http://dx.doi.org/10.1021/acsami.0c08379.

[55] L.J. Frevel, R. Mom, J.-J. Velasco-Vélez, M. Plodinec, A. Knop-Gericke, R. Schlögl, T.E. Jones, In situ X-ray spectroscopy of the electrochemical development of iridium nanoparticles in confined electrolyte, J. Phys. Chem. C 123 (14) (2019) 9146–9152, http://dx.doi.org/10.1021/acs.jpcc.9b00731.

[56] L.J. Frevel, R. Mom, J.-J. Velasco-Vélez, M. Plodinec, A. Knop-Gericke, R. Schlögl, T.E. Jones, Correction to "In situ X-ray spectroscopy on the electrochemical development of iridium nanoparticles in confined electrolyte", J. Phys. Chem. C 124 (27) (2020) 14941–14943, http://dx.doi.org/10.1021/acs.jpcc.0c05226.

[57] J.-J. Velasco-Vélez, L.J. Falling, D. Bernsmeier, M.J. Sear, P.C.J. Clark, T.-S. Chan, E. Stotz, M. Hävecker, R. Kraehnert, A. Knop-Gericke, C.-H. Chuang, D.E. Starr, M. Favaro, R.V. Mom, A comparative study of electrochemical cells for in situ x-ray spectroscopies in the soft and tender x-ray range, J. Phys. D: Appl. Phys. 54 (12) (2021) 124003, http://dx.doi.org/10.1088/1361-6463/abd2ed.

[58] M. Teliska, W.E. O'Grady, D.E. Ramaker, Determination of o and OH adsorption sites and coverage in situ on Pt electrodes from Pt L23 X-ray absorption spectroscopy, J. Phys. Chem. B 109 (16) (2005) 8076–8084, http://dx.doi.org/10.1021/jp0502003.

[59] C. Roth, N. Benker, T. Buhrmester, M. Mazurek, M. Loster, H. Fuess, D.C. Koningsberger, D.E. Ramaker, Determination of O[H] and CO coverage and adsorption sites on PtRu electrodes in an operating PEM fuel cell, J. Am. Chem. Soc. 127 (42) (2005) 14607–14615, http://dx.doi.org/10.1021/ja050139f.

[60] M. Teliska, V.S. Murthi, S. Mukerjee, D.E. Ramaker, Site-specific vs. specific adsorption of anions on Pt and Pt-based alloys, J. Phys. Chem. C 111 (26) (2007) 9267–9274, http://dx.doi.org/10.1021/jp071106k.

[61] F.J. Scott, S. Mukerjee, D.E. Ramaker, CO coverage/oxidation correlated with PtRu electrocatalyst particle morphology in 0.3 M methanol by in situ XAS, J. Electrochem. Soc. 154 (5) (2007) A396, http://dx.doi.org/10.1149/1.2709496.

[62] M. Prokop, T. Bystron, K. Bouzek, Electrochemistry of phosphorous and hypophosphorous acid on a Pt electrode, Electrochim. Acta 160 (2015) 215–218, http://dx.doi.org/10.1016/j.electacta.2015.01.097.

[63] M. Prokop, T. Bystron, M. Paidar, K. Bouzek, H_3PO_3 electrochemical behaviour on a bulk Pt electrode: adsorption and oxidation kinetics, Electrochim. Acta 212 (2016) 465–472, http://dx.doi.org/10.1016/j.electacta.2016.07.045.

[64] H. Lin, Z. Hu, K.H. Lim, S. Wang, L.Q. Zhou, G. Zhu, K. Okubo, C. Ling, Y.S. Kim, H. Jia, High-temperature rotating disk electrode study of platinum bimetallic catalysts in phosphoric acid, ACS Catal. 13 (8) (2023) 5635–5642, http://dx.doi.org/10.1021/acscatal.3c00432.

[65] V. Domin, M. Prokop, T. Bystron, M. Gatalo, L. Pavko, N. Hodnik, B.F. Gomes, L.C.M. S., C.E. Hartwig, C. Roth, M. Paidar, K. Bouzek, Performance and stability of PtCo alloy catalysts in high-temperature polymer electrolyte membrane fuel cells, Electrochim. Acta 536 (2025) 146707, http://dx.doi.org/10.1016/j.electacta.2025.146707.

[66] R. Mazzaro, A. Piccioni, M. Salvi, P. Vecchi, M. Mazzanti, S. Caramori, F. Boscherini, L. Pasquini, Operando x-ray absorption spectroscopy unveils light-driven redox dynamics at the semiconductor/cocatalyst interface, Sci. Adv. 11 (38) (2025) eadx8089, http://dx.doi.org/10.1126/sciadv.adx8089.

[67] E.G. Ciapina, S.F. Santos, E.R. Gonzalez, Electrochemical CO stripping on nanosized Pt surfaces in acid media: A review on the issue of peak multiplicity, J. Electroanal. Chem. 815 (2018) 47–60, http://dx.doi.org/10.1016/j.jelechem.2018.02.047.

[68] J.S. Spendelow, J.D. Goodpaster, P.J.A. Kenis, A. Wieckowski, Mechanism of CO oxidation on pt(111) in alkaline media, J. Phys. Chem. B 110 (19) (2006) 9545–9555, http://dx.doi.org/10.1021/jp060100c.

[69] B.F. Gomes, M. Prokop, T. Bystron, R. Loukrakpam, C.M. Lobo, M. Kutter, T.E. Günther, M. Fink, K. Bouzek, C. Roth, Effect of phosphoric acid purity on the electrochemically active surface area of Pt-based electrodes, J. Electroanal. Chem. 918 (2022) 116450, http://dx.doi.org/10.1016/j.jelechem.2022.116450.

[70] R.E. Wibowo, R. Garcia-Diez, T. Bystron, M. van der Merwe, M. Prokop, M.D. Arce, A. Efimenko, A. Steigert, M. Bernauer, R.G. Wilks, K. Bouzek, M. Bär, Elucidating the complex oxidation behavior of aqueous H3PO3 on Pt electrodes via in situ tender X-ray absorption near-edge structure spectroscopy at the P K-edge, J. Am. Chem. Soc. 146 (11) (2024) 7386–7399, http://dx.doi.org/10.1021/jacs.3c12381.

[71] L. Breiman, Random forests, Mach. Learn. 45 (1) (2001) 5–32, http://dx.doi.org/10.1023/A:1010933404324.

[72] R.Q. Albuquerque, F. Rothenhäusler, P. Gröbel, H. Ruckdäschel, Multi-objective optimization of sustainable epoxy resin systems through Bayesian optimization and machine learning, ACS Appl. Eng. Mater. 1 (12) (2023) 3298–3308, http://dx.doi.org/10.1021/acsaenm.3c00590.